Observations of OH-airglow from ground, aircraft, and satellite: investigation of wave-like structures before a minor stratospheric warming

Sabine Wüst[1*], Carsten Schmidt[1], Patrick Hannawald[2], Michael Bittner[1,2], Martin G. Mlynczak[3], James M. Russell III[4]

[1] Deutsches Fernerkundungsdatenzentrum, Deutsches Zentrum für Luft- und Raumfahrt, , 82234 Oberpfaffenhofen, Germany
[2] Institut für Physik, Universität Augsburg, Augsburg, Germany
[3] NASA Langley Research Center, Hampton, USA
[4] Center for Atmospheric Sciences, Hampton, USA

Correspondence to: Sabine Wüst (sabine.wuest@dlr.de)

Abstract

In January and February 2016, the OH-airglow camera system FAIM (Fast Airglow Imager) measured during six flights on board the research aircraft FALCON in Northern Scandinavia. Flight 1 (14th January 2016) covering the same ground track in several flight legs and flight 5 (28th January 2016) along the shoreline of Norway are discussed in detail in this study. The images of the OH-airglow intensity are analysed with a two-dimensional FFT regarding horizontal periodic structures between 3 km and 26 km horizontal wavelength and their direction of propagation. Two ground-based spectrometers (GRIPS, Ground based Infrared P-branch Spectrometer) provided OH-airglow temperatures. One was placed at ALOMAR, Northern Norway (Arctic Lidar Observatory for Middle Atmosphere Research; 69.28° N, 16.01° E) and the other one at Kiruna, Northern Sweden (67.86° N, 20.24° E). Especially during the last third of January 2016, the weather conditions at Kiruna were good enough for the computation of nightly means of gravity wave potential energy density. Coincident TIMED-SABER (Thermosphere Ionosphere Mesosphere Energetics Dynamics, Sounding of the Atmosphere using Broadband Emission Radiometry) measurements complete the data set. They allow for the derivation of information about the Brunt-Väisälä frequency and about the height of the OH-airglow layer as well as its thickness.

The data are analysed with respect to the temporal and spatial evolution of mesopause gravity wave activity just before a minor stratospheric warming at the end of January 2016. Wave events with periods longer (shorter) than 60 min might mainly be generated in the troposphere (at or above the height of the stratospheric jet). Special emphasize is put on small-scale signatures, i.e. on ripples, which are signatures of local instability and which may be related to a step in a wave breaking process. The most mountainous regions are characterized by the highest occurrence rate of wave-like structures in both flights.

1 Introduction

The results presented here are part of the international initiative ROSMIC (Role Of the Sun and the Middle atmosphere/ thermosphere/ionosphere In Climate) and the German program ROMIC (Role Of the Middle atmosphere In Climate). One
5 goal of ROMIC was to investigate coupling mechanisms which connect atmospheric layers from the ground up to the top of the middle atmosphere and vice versa. The project GW-LCYCLE, which was part of ROMIC, addressed questions concerning the life cycle of gravity waves, i.e. their excitation, propagation, and dissipation.

During the field campaign in winter 2015/16 in Northern Scandinavia, ground-based as well as airborne airglow measurements were conducted. At the ground, two spectrometers (GRIPS, Ground based infrared P-branch spectrometer,
10 one at Kiruna, 67.86° N, 20.24° E, and one at ALOMAR, Arctic Lidar Observatory for Middle Atmosphere Research; 69.28° N, 16.01° E) and one camera (FAIM, Fast Airglow Imager, at Kiruna) were operated. An additional FAIM system with small aperture was mounted at the DLR (Deutsches Zentrum für Luft- und Raumfahrt) research airplane FALCON. Six flights were conducted in January and February 2016 in Northern Scandinavia. The airglow observations refer to the height range of ca. 80–90 km, all other airborne measurements address heights of ca. 20 km and below. Flight 1 (14th January 2016)
15 covering the same ground track in several flight legs and flight 5 (28th January 2016) with a long flight leg almost parallel to the shoreline of Norway allow for the discussion of different wave activity features and were therefore chosen for a detailed discussion in this study.

In contrast to the airglow imaging system (AMTM, Advanced Mesosphere Temperature Mapper) used by Pautet et al. (2016) during the DEEPWAVE campaign above New Zealand, the airborne FAIM does not allow for the derivation of OH
20 rotational temperatures. The FAIM was optimized for the study of small-scale features in airglow intensity and therefore it has a significantly smaller aperture and covers a wider spectral range from 0.9 μm to 1.65 μm resulting in a higher spatial and temporal resolution at the sacrifice of geographical coverage (Hannawald et al., 2016). While Pautet et al. (2016) analysed a specific gravity wave event, we concentrate here on the temporal and spatial development of periodic structures in the range of ripples and bands during the two flights mentioned above (section 4.2.2 and 5).

25 Information about the temporal development of the potential energy density of larger-scale gravity waves are derived based on the GRIPS measurements at Kiruna (section 4.2.1 and 5). Due to varying weather conditions the temporal resolution of the time series is best during the last third of January 2016. Unfortunately, the weather conditions did not allow these analyses during the same time period for the ALOMAR GRIPS data.

For the calculation of the density of wave potential energy, we compute the (angular) Brunt-Väisälä frequency based on
30 coincident TIMED-SABER (Thermosphere Ionosphere Mesosphere Energetics Dynamics, Sounding of the Atmosphere using Broadband Emission Radiometry) temperature and OH-B channel volume emission rate (VER) measurements. We use the latter also in order to learn more about the OH-layer height and thickness (section 4.1 and 5).

All results are interpreted in the context of the minor stratospheric warming which happened at the end of January 2016 (Dörnbrack et al., 2018).

2   Data

2.1   GRIPS

During winter 2015/16, ground-based airglow observations were carried out with the infrared spectrometers GRIPS 9 at Kiruna (67.86° N, 20.24° E), Sweden and GRIPS 14 at ALOMAR (Arctic Lidar Observatory for Middle Atmosphere
5   Research; 69.28° N, 16.01° E), Norway. GRIPS instruments observe the OH(3-1) and the OH(4-2) vibrational transitions in the spectral range between 1.5 µm and 1.6 µm. In standard setup, the temporal resolution is 15 s (Schmidt et al. 2013). Rotational temperatures are derived operationally from the OH(3-1) P-branch. They typically exhibit uncertainties of ±8 K at this temporal resolution, but the exact value strongly depends on the emission intensity, which can be highly variable. Airglow observations are only performed during darkness and dense cloud coverage poses an obstacle for the measurements.
10   At Kiruna, GRIPS 14 observed the airglow layer at a fixed zenith angle of 0°. Its field of view (FoV) was approximately 25 km x 25 km. GRIPS 9 at ALOMAR was operated in a scanning mode (the FoV is changed four times within one minute then starting with the first one again) with one FoV in zenith direction. Concerning the size of the FoV, the time series referring to zenith direction at ALOMAR is comparable to the measurements at Kiruna. For more information about the GRIPS system, operated in standard and in scanning mode, see Schmidt et al. (2013), Wachter et al. (2015), and Wüst et al.
15   (2018).

Observations at ALOMAR were performed between December 5, 2015 and February 3, 2016. Observations at Kiruna were carried out between January 14 and February 2, 2016. During the latter time period, the weather at ALOMAR was very variable. Information about gravity wave potential energy density according to Wüst et al. (2016) and the data quality criteria given therein were therefore not derived for ALOMAR. Nightly-mean temperatures, however, were successfully retrieved
20   for 56 out of 61 nights at ALOMAR and for 19 out of 19 nights at Kiruna.

2.2   FAIM

Two-dimensional airglow observations were performed by FAIM (Fast Airglow Imager, for details about the ground-based instrument see Hannawald et al., 2016) on board of the DLR aircraft FALCON. The spectral range is 0.9 µm–1.65 µm, the
25   integration time is 1 s, the sensor size is 320 px x 256 px. Due to limited available space, the instrument was mounted at the headmost aperture plate position of the aircraft. The observations were performed in near zenith direction (roll angle of the instrument w.r.t. the aircraft plane: -5°). The aperture angle of the optics was mainly limited by the small diameter window (approx. 70 mm), so a lens system with opening angles of 27.3° x 33.9° was used (larger angles resulted in stronger vignetting). In order to maximise the geographical coverage, the camera was mounted with a yaw angle of -45°, making the
30   image diagonally oriented to the flight track (compare Fig. 7 and 10). The spatial resolution was approximately 167 meters per pixel, the FoV covered an area of 43 km x 55 km. The exact values depend on the roll, yaw and pitch angles as well as

on the height of the aircraft. The high temporal and spatial resolution allows especially the investigation of gravity waves with short wavelengths and short periods along the flight track.

During the GW-LCYCLE campaign, six night-time flights were conducted above Northern Scandinavia. At least large parts of the flights took place above the tropospheric cloud level. The camera delivered data for all six flights. Flight 1 (14th
5   January 2016) and flight 5 (28th January 2016) were least disturbed by aurora or moon light. Therefore, they are subject of this study.

Additionally, an all-sky FAIM system was operated at Kiruna from January, 14th 2016 to February, 2nd 2016. Due to low level clouds or fog at the times of the aircraft overpasses as well as some water vapour condensation occurring on the entrance optics during the very cold nights (-40°C), only few nights of this ground-based imager can be analysed. Therefore,
10 these measurements are not subject of further analysis here.

2.3   TIMED-SABER

The TIMED satellite was launched on 7 December 2001 and the on-board limb-sounder SABER delivers vertical profiles of
15 kinetic temperature on a routine base from approximately 10 km to more than 110 km altitude with a vertical resolution of about 2 km until today. The high vertical resolution is suitable for the investigation of gravity wave activity. About 1200 temperature profiles are available per day. The latitudinal coverage on a given day extends from about 53° latitude in one hemisphere to 83° in the other. Due to 180° yaw manoeuvres of the TIMED satellite this viewing geometry alternates once every 60 days (Mertens et al., 2004; Mlynczak, 1997; Russell et al, 1999). A variety of SABER publications is available, and
20 an overview is given on http://saber.gats-inc.com/publications.php.

Kinetic temperatures are derived from the 15 μm CO_2 emissions. One of the main problems of deducing kinetic temperature values in the mesosphere and upper levels is certainly non-LTE conditions (NLTE), i.e. conditions that depart from Local Thermodynamic Equilibrium. NLTE algorithms for kinetic temperature were employed in the SABER temperature retrieval in version 1.03 (Lopez-Puertas et al., 2004) as well as in versions, 1.04 and 1.06 (Mertens et al., 2004, 2008). In version 1.07
25 further improvements were made: CO_2 profiles from the Whole Atmosphere Community Climate Model (WACCM) are used in the retrieval algorithm in order to remove inconsistencies in the vertical structure of diurnal temperature tides (Remsberg et al., 2008), for example.

Comparisons with reference data sets generally confirm the good quality of SABER temperatures. In the stratosphere and lower mesosphere biases of 1 K to 3 K are indicated (SABER temperatures are too high by 2–3 K in the lower stratosphere,
30 too low by 1 K in the upper stratosphere and by 2–3 K in the mid-mesosphere). Due to noise effects, increased uncertainties have to be expected in the UMLT region. Comparisons to LIDAR and airglow measurements show differences of 10 K and more (Remsberg et al., 2008).

We use TIMED-SABER temperature and OH-B channel data (volume emission rates, VER) in its latest version (2.0) within a square of 300 km edge length centred at ALOMAR and between 17 and 5 UTC for the derivation of additional information about the OH-airglow layer characteristics and about the (angular) Brunt-Väisälä (BV) frequency at mesopause height. These values are also taken for Kiruna, since both locations are not more than 300 km away from each other. The OH-B

5 channel covers the wavelength range from 1.56 to 1.72 μm, which includes mostly the OH(4-2) and OH(5-3) vibrational transition bands. The mean height difference between the OH(4-2)- and the OH(3-1)-emission, which is addressed by the OH*-spectrometers mentioned above, is approximately 500 m (von Savigny et al., 2012) and therefore negligible compared to the FWHM.

The data was downloaded from the SABER homepage (saber.gats-inc.com).

3   Analysis

3.1   Derivation of wave potential energy density

From the GRIPS data, we derive the density of gravity wave potential energy E_{pot} (GWPED) according to

$$E_{pot} = \frac{1}{2}\frac{g^2 \overline{\hat{T}'^2}}{N^2} \tag{1}$$

5   where

g is the acceleration of gravity, (g=9.6 m/s² taking into account its height-dependence),

N the (angular) BV frequency, and

$\hat{T}' = T'/\hat{T}$ the normalized temperature fluctuation. The overbar denotes the nightly average.

10   E_{pot} is calculated for different period ranges (shorter and longer than 60 min). Details can be looked up in Wüst et al. (2016).
For the derivation of the (angular) BV frequency N vertically-resolved temperature profiles are needed:

$$N = \sqrt{\frac{g}{T}\left(\frac{dT}{dz} + \Gamma\right)} \tag{2}$$

where

z is the height,

15   T is the temperature and

Γ the dry adiabatic lapse rate with 9.6 K/km.

Since GRIPS provides a temperature value which is vertically averaged over the OH*-layer, additional data are necessary.
As in Wüst et al. (2016, 2017a, 2017b), TIMED-SABER temperature information are used for this purpose. The OH*-
20   equivalent (angular) BV frequency is calculated for the day of year (DoY) 1–60 of 2016 by weighting the height-dependent
squared BV-frequency values with the volume emission rate (VER) profiles. From time to time, the maximum of the VER is
observed around 40 km in SABER profiles. Therefore, the calculation is restricted to the height range between 71 and 97 km
(84 km ± 13 km, the height of 84 km corresponds to the mean OH*-layer height derived by Wüst et al., 2016). Since the
SABER profile provides only a snapshot of the atmospheric situation, an error of 10% is assumed. This value catches the
25   day-to-day variability (Wüst et al., 2017b).

3.2 Spectral analysis

In order to analyse the FAIM measurements, a two-dimensional Fast Fourier Transform (2D FFT) is applied. Sequences with high roll and pitch angles as they occur during turning manoeuvres were excluded since the size of the FoV and the spatial resolution change significantly within a short time. A steady shaking of the airplane limits the application of the 2D FFT: phase information of consecutive images cannot be used to derive additional parameters such as period and phase speed. Only horizontal wavelength and the direction of propagation with a 180° ambiguity are computed.

The used 2D FFT algorithm needs equidistant data. Therefore, the images are un-warped. As mentioned above, the camera is deployed at a roll angle w.r.t. the plane of -5° and at a yaw angle w.r.t. the plane of -45°. Therefore, two rotation matrices (one for the yaw axis and one for the roll axis) are used to convert the reference system of the instrument to the reference system of the airplane. The orientation of the airplane is also characterized by a roll, pitch, and yaw angle. Therefore, three rotation matrices are then applied to transform the reference system of the airplane to a world coordinate system (azimuth and elevation relative to the Earth's surface). The three required angles are taken from the flight metadata which are given with a temporal resolution of 1 s. The new pixel positions are then calculated by projecting the image in world coordinates to the airglow layer at 87 km height. Changes in the airglow layer altitude have only minor effects on the results. An additional flipping at the North-South axis brings the image to a satellite's view perspective. The scale is kept constant with 167 m/px (or 6 px/km) for all images allowing direct comparison of images at different times and angles. Before analysing the un-warped images, the stars in the images need to be removed since otherwise their signal may influence the 2D FFT spectra. This is done by applying a sliding median blur with a kernel of 17 x 17 px.

All images are cropped to 26 km x 26 km. This is the largest square size which does not contain any pixels outside the un-warped image region (marked in Fig. 1).

For each image, the mean is subtracted and a Kaiser-Bessel window ($\alpha=4$) is applied to let the borders of the area steadily decrease to zero. Zero-padding further optimises the calculation of the 2D-FFT.

After calculating the 2D FFT for each image (each flight consists of ca. 12,000 images), wavelength and angle of propagation are extracted for every significant peak in the spectrum (Monte-Carlo significance test with a significance level of 95%).

The algorithm is described in detail in Hannawald et al. (2018).

4 Results

4.1 Height, thickness and intensity of the OH-layer

During winter (DoY 1–60) 2002–2016, the maximum of the volume emission rate, in the following denoted as OH*-layer height, and its full-width a half maximum (FWHM) around ALOMAR vary between ca. 80.0–88.0 km and 6.0–10.5 km,

5 respectively (see Fig. 2 (a) and (b) for a comparison with all other years, and Fig. 3 (a) and (b) for details about the year 2016). Compared to all other years, the FHWM for 2016 (thick blue line) can be characterized as low especially during the end of January and large parts of February. It shows a drop centred at DoY 43. The OH*-layer height is stable at 85.0–85.5 km until DoY 23 and starts to rise by 2.5 km during the following ten days. Afterwards, it varies around ca. 87.5 km. Compared to all other years, the OH-airglow layer increases and its width decreases from DoY 23 on.

10 Both, ground-based GRIPS and space borne SABER observations of the OH intensity, agree fairly well during the GW-LCYCLE campaign (see Fig. 4a). In particular, they show a pronounced periodicity of ca. 4–6 days. At the end of January and the beginning of February, the intensity reaches its absolute minimum. The same characteristics hold also for the temperature derived by GRIPS at ALOMAR and Kiruna (see Fig. 4b).

4.2 Periodic signatures

4.2.1 Horizontal wavelengths longer than ca. 25 km

Due to the FoV of GRIPS 9 at Kiruna, the instrument is sensitive to horizontal wavelengths of 25 km and longer. As mentioned in section 3.1, the OH*-equivalent (angular) BV frequency is calculated based on SABER temperature

20 measurements in order to compute GWPED from GRIPS. Between day 1 and 60 of 2016, the OH*-equivalent (angular) BV frequency decreases nearly linearly from approximately 0.023 1/s to 0.021 1/s (Fig. 5, dashed line) showing superimposed fluctuations which reach ca. 13% deviation from the linear fit at maximum.

According to the data quality criteria for the GWPED calculation as mentioned in Wüst et al. (2016), information about the

25 energy content of gravity waves are derived between the nights from 13th to 14th and 30th to 31st January, 2016.

For periods longer (shorter) than 60 min, the energy density varies between 10 and 160 J/kg (5 and 17 J/kg) with a mean of 43 J/kg (9 J/kg) (Fig. 6). Relative to these means, individual values lie within an interval of -77% and + 192% (-38% and +45%) for long (short) periods. The potential energy density of gravity waves with periods longer than 60 min can therefore

30 be characterized as being more variable compared to periods shorter than 60 min. Fitting a cubic spline (non-iterative version as described in Wüst et al., 2017c) to the GWPED values suggests that a minimum of GWPED is observed around January

21st and 22nd and a maximum around January 27th for periods longer than 60 min. This overall behaviour cannot be confirmed for periods shorter than 60 min.

4.2.2   Horizontal wavelengths shorter than ca. 25 km

Wavelengths shorter than 25 km can be analysed using data of the airborne FAIM. The route of the first flight forms a triangle with the last two flight legs parallel to a circle of longitude and latitude. The diagonal connection between Kiruna and approximately ALOMAR was covered three times in a row (Fig. 7). Although this flight track allows in principal the investigation of horizontal structures much larger than the FAIM FoV (via comparison of the individual flight legs), the airglow brightness varied too fast during the entire flight for achieving unambiguous results. This is especially apparent in the diagonal flight legs (Fig. 8a). Therefore, we concentrate on the analysis of horizontal structures in the range of the FoV size. As mentioned in section 2.2, the FoV is ca. 43 km x 55 km at 90 km height. However, its size changes with varying roll and pitch angles.

Figure 7 shows time difference images (time difference: 10 s) of the first flight. The velocity of the airplane is approximately 210 m/s. So, the airplane moves ca. 2 km in 10 s. Calculating a difference image emphasizes horizontal structures which change significantly within 2 km and/or within 10 s in flight direction. In the case of gravity waves, the result depends on the horizontal wavelengths and on the horizontal phase speed. For gravity waves with zero phase speed, constructive interference appears for a horizontal wavelength of 4 km in flight direction. The longer the wavelength, the less it will be emphasized. Destructive interference happens for horizontal wavelengths of 2 km (divided by integer factors) in flight direction. However, the above-mentioned constant shaking of the aircraft aids that also these small structures can at least to some extent be identified in the images. So, one can say calculating a difference image is equivalent to applying some (high-pass) spectral filtering and amplification algorithm. The difference images of the first flight show wave-like structures of different wavelengths and amplitudes. There exists almost no region where such structures cannot be observed.

In order to derive quantitative results, the original (non-difference) images are analysed with a 2D FFT. Details about the different analysis steps are given in section 3.2. The shortest wavelength to which the FFT in sensitive is ca. 3 km (due to pre-processing with median blur applied to 17 pixels, 6 pixels correspond to 1 km). The FoV is cut to 26 km x 26 km.

It becomes clear that wave numbers and intensities vary in time and space (see Fig. 8b). In flight 1, high Fourier amplitudes also in the range of small-scale features appear approximately between 16:20 UTC and 16:35 UTC (flight leg 1, turning manoeuver needs to be excluded) and between 17:30 and 18:00 UTC (flight leg 2 and 3). Between 18:30 UTC and 18:55 UTC (flight leg 4 and 5) especially small-scale features are relatively pronounced while larger-scale features are weaker compared to the time periods just mentioned. During these three time periods, the airplane was located east and/or

southeast as well as above the Scandinavian mountain chain. The airglow brightness averaged over each picture shows local maxima during these three time periods (Fig. 8a).

Summarized over the whole flight, structures with wavelengths longer than 15 km propagate more frequently to the southeast (and/or northwest) than to the northeast (and/or southwest, Fig. 9). The majority of wavelengths shorter than 15 km

5   moves to the northeast (and/or southwest).

During the fifth flight on January 28th, 2016, airglow observations were performed on the return from Karlsbad, Southern Sweden, over Bergen, Southern Norway, along the coast line of Norway back to Kiruna (Fig. 10). The flight route can be divided into three legs. Several oscillations with 20–25 km are clearly visible at the beginning and at the end of the flight

10 track. Especially, during the second (latitude-parallel) leg, many superimposed small structures with different orientations can be seen. The airglow intensity averaged over each image shows wave-like structures during each flight leg (Fig. 11a). They are most pronounced in flight leg 3. The horizontal wavelengths (in flight direction) reach 75–100 km (from Fig. 11a under the assumption that the phase speed of the wave is negligible w.r.t. the speed of the plane with ca. 210 m/s).

Regions characterized by pronounced wave activity are observed especially after 18:30 UTC (Fig. 11b, mostly flight leg 3).

15 During this time, the airplane flew along the coast line of Norway or above the Scandes. In contrast to flight 1, airglow brightness (averaged over each image) is maximal before the time period of maximal (Fourier) intensity.

Flight 5 also differs from flight 1 concerning the propagation directions (Fig. 12): wavelengths longer than 15 km propagate mostly to the northeast (and/or southwest), for wavelengths shorter than 15 km a preferred quadrant of propagation cannot be identified. A pronounced maximum can be found for eastward (and/or westward) propagation direction. In this direction

20 nearly no larger-scale waves move.

The occurrence rate of wave events varies during one flight and from flight to flight (Fig. 13). Overall, the legs of flight 5 show less variability than the legs of flight 1.

For both flights, the zonal legs (leg 5 of flight 1 and leg 2 of flight 5), where the airplane flew most of the time over the

25 mountain chain and passed the highest elevations of the respective flight routes (grey line in Fig. 8a and 11a), are characterized by the highest occurrence rate (ca. factor 1.8–4.5 enhanced compared to the leg with the lowest occurrence rate of the respective flight). This agrees quite well with the visual inspection of the difference images of flight 5 (Fig. 10). For flight 1, this result is due to a large portion of small-scale wave-like structures (3–15 km wavelength) in leg 5.

The diagonal legs 1, 2 and 3 of flight 1 are identical concerning the route, however, the occurrence rate varies: it is highest in

30 leg 2 and lowest in leg 3 (factor of ca. 2.6).

5   Discussion

Stratospheric winds varied strongly during the January 2016 (Fig. 14). This was due to a minor stratospheric warming at the end of January (Dörnbrack et al., 2018). The polar vortex was displaced southward with its centre between Svalbard and
5   Northern Scandinavia and the polar night jet became elongated in west-east direction (strong curvature over the Northern Atlantic and over Siberia). A stratospheric warming should affect the residual circulation and therefore the OH-layer characteristics. When stratospheric winds weaken or even reverse, filtering of gravity waves generated further down is changed. When there is a stratospheric wind weakening or reversal, the downward movement in the mesopause, which is part of the residual circulation, weakens and this influences the OH excitation mechanism. However, planetary wave activity
10   complicates this simplified picture: transmission of gravity waves is then a function of longitude (Whiteway and Carswell (1994), Dunkerton and Butchart (1984), and references in both publications).

Neglecting the effect of planetary waves, we expect the following. The OH excitation mechanism is dominated by atomic oxygen which is produced at higher altitudes in the atmosphere (Shepherd et al., 2006). Processes which lead to vertical transport of atomic oxygen influence the OH volume emission rate, but also height and thickness of the OH*-layer (see also,
15   Liu and Shepherd, 2006; Mulligan et al., 2009). On average, height and thickness as well as height and intensity are anti-correlated. So, a weakening of the residual circulation should lead to a higher OH-airglow altitude, to a thinner OH-airglow layer, to a reduced OH-airglow intensity, and to a lower temperature. The temporal development of the airglow-layer characteristics observed at the end of January 2016 is consistent with the described expectations before and during a stratospheric warming.

Additional to the OH-layer characteristics, we also analysed periodic structures of different horizontal wavelengths. In literature, wave-like horizontal structures are often divided into ripples and bands. Ripple structures are phenomena with horizontal wavelengths of 5–15 km (Li et al., 2005, Taylor et al., 1995) or of 20 km at most (Takahashi et al., 1985). Their lifetime is in the range of 45 min and less (Hecht, 2004). Fronts with large horizontal extent and wavelength, which can be
25   sometimes observed for hours, are usually called bands (Taylor et al., 1995; Clairemidi et al., 1985). Hecht (2004) summarizes in his table 1 band and ripple characteristics based on four literature studies: the observed periods of ripples (close to 5 min) are shorter than the ones for the bands, this also holds for the horizontal wavelengths. However, the provision of exact values does not seem to be possible.

Ripples are interpreted as signatures of local instability and may be related to or also be part of a breaking process of an
30   atmospheric gravity wave (Li et al., 2005). They move with the background wind and can be separated into convective and dynamical ones according to their generation process (convective and dynamical instability, which occur for a Richardson number of less than 0 and 0–0.25, respectively). Ideally, the phase fronts of the dynamical (convective) ripples are oriented parallel (perpendicularly) to the associated gravity wave. However, also other cases have been observed (Hecht, 2004).

In our airborne measurements, we find horizontal wavelengths in the range of ripples and bands. The chance to measure low-frequency (inertia) waves by FAIM is very much reduced compared to waves with higher frequencies. The higher the intrinsic frequency of a wave, the steeper the wave fronts (with respect to the vertical) are. The horizontal wavelengths derived from the FAIM data are 26 km at maximum. The vertical wavelengths of low-frequency waves are much smaller than the horizontal ones. Since the OH* layer extends over some kilometres, vertical wavelengths in the range of the full width at half maximum can barely be detected (Wüst et al., 2016).

Conclusions about possible sources of the observed bands are very difficult without a ray tracer since wind and temperature change with height influencing the angle of the wave front to the vertical.

However, we can conclude the following. Before January 25th, the stratospheric jet was faster than the tropospheric one above Kiruna (Fig. 14). During January 25th and 28th, the zonal wind in the troposphere and in the stratosphere was of comparable (eastward) velocity. So, for gravity waves generated in the troposphere, the stratospheric jet was not an additional filter. After January 28th, the vertical profile of the zonal wind showed regions of positive and negative wind velocity. An enhanced gravity wave filtering (for waves which had to pass the different regions) could therefore be expected. This agrees with the temporal development of the density of wave potential energy (periods longer than 60 min), which depicts a maximum around the 27th of January (Fig. 6). For gravity waves with periods shorter than 60 min, the temporal development shows less and different variations. Therefore, we conclude that gravity waves with periods longer than 60 min could to a larger part be generated in the troposphere than gravity with periods shorter than 60 min.

We can argue that especially mountain waves (phase velocity equal to zero) generated near Kiruna had the best chance to reach the OH-airglow layer around January 21st and from January 24th to 28th. During the other time periods, the horizontal wind speed became zero in extended height intervals (Fig. 14), which prohibits a vertical propagation (Fritts and Alexander, 2003). Indeed, we observed the highest occurrence rate of band-like structures during flight 5 (January 28th) when the airplane flew most of the time over the mountain chain and passed the highest elevations of the flight route.

Generally, we can conclude that at the end of January the source of high- and medium-frequency waves generated in the lower troposphere would be at a horizontal distance of ca. 90 km height and more from the measurement place. During this time, the wind profile is rather flat, so the intrinsic frequency is approximately equal to the ground-based frequency and the vertical wavelength does not vary much with height (only due to the changing (angular) BV frequency). If we assume that wave fronts of high- and medium frequency waves are oriented 0–45° to the vertical and if we take into account that our measurements address ca. 90 km height, then the possible tropospheric source must be ca. 90 km and more away from Kiruna.

In order to find out more about the different kinds of ripples, which we probably observed in the two flights, we need information about horizontal wind and temperature between 80 km and 100 km. Airborne or comprehensive ground-based measurements of these parameters are not available. Therefore, we do not get precise information about convective and

dynamical instability along the flight track. From the temporal development of the (angular) BV frequency based on TIMED-SABER measurements, we can at least conclude that overall the tendency of the OH-airglow layer height to develop static instability increased during the measurement period. In the following, we try to use the airglow brightness maps to learn more about convective and dynamic instability in the two flights.

5 Since it is winter, the mesopause is located above the OH* layer at ca. 100 km height (e.g., Lübken and Von Zahn, 1991). Thus, the overall vertical temperature gradient is negative in the height range of the OH* layer. Static instability is therefore possible and independent of the existence of gravity waves. However, if gravity waves are present, then the probability for convective instability should change most in the grey regions of an airglow image since the wave-induced absolute temperature gradient is maximal there. This can be explained as follows.

10 The brightness of the OH* layer is mainly determined by the availability of atomic oxygen, which is generated higher up in the atmosphere (Shepherd et al., 2006). All processes which lead to a vertical transport of atomic oxygen therefore influence this parameter. Thus, downward transport processes are more pronounced in brighter areas of OH-airglow images compared to darker ones.

If the vertical transport processes happen adiabatically, e.g. due to a wave, adiabatic warming, i.e., positive temperature
15 deviations from the atmospheric background, should be observed in the brighter parts of an airglow image. Darker airglow regions should then be affected by negative temperature deviations from the atmospheric background. Grey regions should be characterized by nearly no temperature deviation from the atmospheric background. We would like to emphasize here that a strict correlation between airglow brightness and temperature in the sense of the brighter the airglow, the higher the temperature and vice versa does not hold as for example Fig. 7 of Pautet et al. (2014) makes clear. So, if the vertical
20 movements of atomic oxygen are due to a wave, one can conclude that the wave-induced vertical temperature gradient becomes zero where the brightness is maximal or minimal, while the grey regions can be interpreted as the zero-crossings of a wave observed in a vertical temperature profile. There, the steepest absolute vertical temperature gradient exists and the static stability of the atmosphere is most influenced. It can be higher or lower compared to the regions between the zero-crossings.

25 The probability for dynamic instability should change most in the bright and dark regions of an airglow image. This follows from the gravity wave polarization equations: the shear is maximized when the temperature is extreme (Heale et al., 2017).

As mentioned in the previous section, pronounced wave activity, also in the range of small-scale wave-like structures, is observed in bright airglow areas during flight 1. If we assume, that these small-scale structures are ripples and that the generating gravity waves dominate the averaged airglow images then this means that the ripples are mainly due to dynamical
30 instability. For flight 5, the situation is different. Here, pronounced wave activity also of small-scale wave-like structures is not necessarily linked to very bright airglow areas. For example, at the beginning of our measurements, relatively low wave activity can be observed while the airglow brightness shows a broad maximum (Fig. 11). It is followed by a period (around 18:40 UTC–18:45 UTC) during which the airglow brightness is neither maximal nor minimal but relatively high wave

activity is present. Therefore, we conclude that overall the importance of dynamical instability is smaller for this flight compared to the first one.

6   Summary and conclusion

Wave-like structures in the range of ripples and bands, ca. 3–25 km horizontal wavelength, were observed during two selected flights (flight 1 on January, 14th, 2016 and flight 5 on January, 28th, 2016) of the airborne airglow camera FAIM in Northern Scandinavia. The flights were separated by 14 days and took place under different atmospheric conditions: while the stratospheric jet was rather strong during the first flight, it was much weaker during the last one. In the same time, ground-based airglow observations (temperature and intensity) as well as TIMED-SABER based measurements (OH-airglow layer height and thickness) revealed typical features of a stratospheric warming.

The activity of these wave-like structures depended on place and time. Regions of vanishing wave activity could not be observed. The most mountainous regions were characterized by the highest occurrence rate of wave-like structures in both flights. For flight 1, this result is due to a large portion of structures in the range of ripples. At the time of this flight, the propagation of mountain waves was not possible or at least strongly reduced. This is probably not the case for flight 5.

We found hints for a higher probability of convectively-induced ripples in flight 5 compared to flight 1. This agrees with our observations of the static stability of the airglow-layer height during January based on TIMED-SABER.

The wave potential energy referring to waves of ca. 25 km horizontal wavelength and more varied also in time (time period: 14th–30th January) as ground-based airglow observations by GRIPS during January 2016 showed. For waves with periods longer than 60 min, it is characterized by signatures which would be expected for waves generated below the tropospheric jet. This does not hold for waves with periods shorter than 60 min. Therefore, we conclude that wave events with periods longer than 60 min might mainly be generated in the troposphere, while the source of waves with periods shorter than 60 min might mainly be at the height or above the height of the stratospheric jet.

Author contribution

Carsten Schmidt, Patrick Hannawald and Sabine Wüst assured the operability of the ground-based and airborne instruments, GRIPS and FAIM, during the GW-LCYCLE campaign. Martin G. Mlynczak and James M. Russell are responsible for the TIMED-SABER data. Patrick Hannawald, Sabine Wüst and Carsten Schmidt analyzed the data. Sabine Wüst and Michael

5   Bittner formulated the respective research goals in the proposal GW-LCYCLE. Sabine Wüst wrote the manuscript and discussed it especially with Michael Bittner, Patrick Hannawald and Carsten Schmidt.

Competing Interests

The authors declare that they have no conflict of interest.

Acknowledgement

For the overall organization of the flight campaign, we thank our colleagues from DLR, especially Markus Rapp and Andreas Dörnbrack, institute of atmospheric physics (IPA). For the acquisition of the project GW-LCYCLE, we thank Markus Rapp. Verena Wendt and Jeng-Hwa Yee deserve gratitude for her preparatory work concerning the SABER data

15   analysis.

We thank the German Ministry for Education and Research (BMBF, Grant agreement No: 01LG1206A) for funding. Some algorithms applied in this study were developed in the VAO-project LUDWIG which was funded by the Bavarian State Ministry for the Environment and Consumer Protection (project number TUS01 UFS-67093).

Processing and long-term archiving of the FAIM and GRIPS data is provided by the World Data Center for Remote Sensing

20   of the Atmosphere (WDC-RSAT, http://wdc.dlr.de). The measurements are part of the Network for the Detection of Mesospheric Change, NDMC (https://www.wdc.dlr.de/ndmc).

References

Clairemidi, J., Herse, M., and Moreels, G.: Bi-dimensional observations of waves near the mesopause at auroral latitudes, Planet. Space Sci., 33, 1013–1022, 1985.

Dunkerton, T. J., and Butchart, N.: Propagation and selective transmission of internal gravity waves in a sudden warming. J. Atmos. Sci., 41(8), 1443–1460, 1984.

Dörnbrack, A., Gisinger, S., Kaifler, N., Portele, T., Bramberger, M., Rapp, M., Gerding, M., Söder, J., Žagar, N., and Jelić, D.: Gravity Waves excited during a Minor Sudden Stratospheric Warming, Atmos. Chem. Phys. Discuss., 10.5194/acp-2018-228, in review, 2018.

Fritts, D. C., and Alexander, M. J.: Gravity wave dynamics and effects in the middle atmosphere, Rev. Geophys., 41, 1003, doi: 10.1029/2001RG000106, 2003.

Hannawald, P., Schmidt, C., Wüst, S., and Bittner, M.: A fast SWIR imager for observations of transient features in OH airglow, Atmos. Meas. Tech., 9, 1461–1472, doi:10.5194/amt-9-1461-2016, 2016.

Hannawald, P., Schmidt, C., Sedlak, R., Wüst, S., and Bittner, M.: Seasonal and intra-diurnal variability of small-scale gravity waves in OH airglow at two Alpine stations, submitted to AMT.

Heale, C. J., Bossert, K., Snively, J. B., Fritts, D. C, Pautet, P.-D. and Taylor, M. J.: Numerical modeling of a multiscale gravity wave event and its airglow signatures over Mount Cook, New Zealand, during the DEEPWAVE campaign, J. Geophys. Res. Atmos., 122, 846–860, doi:10.1002/2016JD025700, 2017.

Hecht, J. H.: Instability layers and airglow imaging. Rev. Geophys., 42(1), 2004.

Li, T., She, C. Y., Williams, B. P., Yuan, T., Collins, R. L., Kieffaber, L. M., & Peterson, A. W.: Concurrent OH imager and sodium temperature/wind lidar observation of localized ripples over northern Colorado. J. Geophys. Res. Atmos., 110(D13), 2005.

Liu, G. and Shepherd, G. G.: An empirical model for the altitude of the OH nightglow emission. Geophys. Res. Lett., 33(9), 2006.

López-Puertas, M., Garcia-Comas, M., Funke, B., Picard, R. H., Winick, J. R., Wintersteiner, P. P., Mlynczak, M. G., Mertens, C. J., Russell III, J. M., and Gordley, L. L.: Evidence for an OH (v) excitation mechanism of CO_2 4.3 μm nighttime emission from SABER/TIMED measurements, J. Geophys. Res., 109, D09307, doi: 10.1029/2003JD004383, 2004.

Lübken, F.-J., and von Zahn, U.: Thermal structure of the mesopause region at polar latitudes. J. Geophys. Res. Atmos., 96(D11):20841–20857, 1991.

Mertens, C. J., Schmidlin, F. J., Goldberg, R. A., Remsberg, E. E., Pesnell, W. D., Russell III, J. M., Mlynczak, M. G., López-Puertas, M., Wintersteiner, P. P., Picard, R. H., Winick, J. R., and Gordley, L. L.: SABER observations of mesospheric temperatures and comparisons with falling sphere measurements taken during the 2002 summer MaCWAVE campaign, Geophys. Res. Lett., 31, L03105, doi: 10.1029/2003GL018605, 2004.

Mertens, C. J., Fernandez, J. R., Xu, X., Evans, D. S., Mlynczak, M. G., and Russell III, J. M.: A new source of auroral infrared emission observed by TIMED/SABER, Geophys. Res. Lett., 35, 17–20, 2008.

Mlynczak, M. G.: Energetics of the mesosphere and lower thermosphere and the SABER experiment, Adv. Space Res., 20, 1177–1183, doi: 10.1016/S0273-1177(97)00769-2, 1997.

Mulligan, F. J., Dyrland, M. E., Sigernes, F., and Deehr, C. S.: Inferring hydroxyl layer peak heights from ground-based measurements of OH (6-2) band integrated emission rate at Longyearbyen (78°N, 16°E). Ann. Geophys., 27, 41974205, 2009.

Pautet, P.-D., Taylor, M. J., Pendleton, W. R., Zhao, Y., Yuan, T., Esplin, R., and McLain, D.: Advanced mesospheric temperature mapper for high-latitude airglow studies. Appl. Opt., 53(26), 5934–5943, 2014.

Pautet, P.-D., Taylor, M. J., Fritts, D. C., Bossert, K., Williams, B. P., Broutman, D., Ma, J., Eckermann, S. D. and Doyle, J. D.: Large-amplitude mesospheric response to an orographic wave generated over the Southern Ocean Auckland Islands (50.7°S) during the DEEPWAVE project, J. Geophys. Res. Atmos., 121, 1431–1441, doi:10.1002/2015JD024336, 2016.

Remsberg, E. E., Marshall, B. T., Garcia-Comas, M., Krueger, D., Lingenfelser, G. S., Martin-Torres, J., Mlynczak, M. G., Russell III, J. M., Smith, A. K., Zhao, Y., Brown, C., Gordley, L. L., Lopez-Gonzalez, M. J., Lopez-Puertas, M., She, C.-Y., Taylor, M. J., and Thompson, R. E.: Assessment of the quality of the Version 1.07 temperature versus pressure profiles of the middle atmosphere from TIMED/SABER, J. Geophys. Res., 113, D17101, doi: 10.1029/2008JD010013, 2008.

Russell III, J. M., Mlynczak, M. G., Gordley, L. L., Tansock Jr., J. J., and Esplin, R. W.: Overview of the SABER experiment and preliminary calibration results, Proc. SPIE 3756, Optical Spectroscopic Tech. Instrum. Atmos. Space Res. III, 277–288, doi: 10.1117/12.366382, 1999.

Schmidt, C., Höppner, K., Bittner, M.: A ground-based spectrometer equipped with an InGaAs array for routine observations of OH(3-1) rotational temperatures in the mesopause region, J. Atmos. Sol.-Terr. Phys., 102, 125–139, doi: 10.1016/j.jastp.2013.05.001, 2013.

Shepherd, G. G., Cho, Y.-M., Liu, G., Shepherd, M. G., and Roble, R. G.: Airglow variability in the context of the global mesospheric circulation. J. Atmos. Sol.-Terr. Phys. 68(17), 2000–2011, 2006.

Takahashi, H., Batista, P. P., Sahai, Y., and Clemesha, B. R.: Atmospheric wave propagations in the mesopause region observed by the OH (8, 3) band, NaD, O2A (8645Å) band and OI 5577 Å nightglow emissions. Planet. Space Sci., 33(4), 381–384, 1985.

Taylor, M. J., Bishop, M. B., and Taylor, V.: All-sky measurements of short period gravity waves imaged in the OI(557.7 nm), Na(589.2 nm) and near infrared OH and O2(0,1) nightglow emissions during the ALOHA-93 campaign, Geophys. Res. Lett., 22, 2833–2836, 1995.

von Savigny, C., McDade, I. C., Eichmann, K. U., and Burrows, J. P.: On the dependence of the OH* Meinel emission altitude on vibrational level: SCIAMACHY observations and model simulations, Atmos. Chem. Phys., 12, 8813–8828, doi: 10.5194/acp-12-8813-2012, 2012.

Whiteway, J. A., and Carswell, A. I.: Rayleigh lidar observations of thermal structure and gravity wave activity in the high Arctic during a stratospheric warming. J. Atmos. Sci., 51(21), 3122–3136, 1994.

Wachter, P., Schmidt, C., Wüst, S., and Bittner, M.: Spatial gravity wave characteristics obtained from multiple OH(3-1) airglow temperature time series, J. Atmos. Sol.-Terr. Phys., 135, 192–201, doi: 10.1016/j.jastp.2015.11.008, 2015.

Wendt, V., Wüst, S., Mlynczak, M. G., Russell III, J. M., Yee, J.-H., and Bittner, M.: Impact of atmospheric variability on validation of satellite-based temperature measurements. J. Atmos. Sol.-Terr. Phys. 102: 252–260. DOI: 10.1016/j.jastp.2013.05.022, 2013.

Wüst, S., Wendt, V., Schmidt, C., Lichtenstern, S., Bittner, M., Yee, J.-H., Mlynczak, M. G., and Russell III, J. M.: Derivation of gravity wave potential energy density from NDMC measurements, J. Atmos. Sol.-Terr. Phys., 138, 32–46, doi: 10.1016/j.jastp.2015.12.003, 2016.

Wüst, S., Schmidt, C., Bittner, M., Silber, I., Price, C., Yee, J.-H., Mlynczak, M.G., and Russel III, J.M.: First ground-based observations of mesopause temperatures above the Eastern-Mediterranean Part II: OH*-climatology and gravity wave activity. J. Atmos. Sol Terr. Phys., 155, 104–111, doi: 10.1016/j.jastp.2017.01.003, 2017a.

Wüst, S., Bittner, M., Yee, J.-H., Mlynczak, M. G., and Russell III, J. M.: Variability of the Brunt-Väisälä frequency at the OH*-layer height, Atmos. Meas. Tech., 10, 4895–4903, doi: 10.5194/amt-10-4895-2017, 2017b.

Wüst, S., Wendt, V., Linz, R., and Bittner, M.: Smoothing data series by means of cubic splines: quality of approximation and introduction of a repeating spline approach. Atmos. Meas. Tech., 10, 3453–3462, doi: 10.5194/amt-10-3453-2017, 2017c.

Wüst, S., Offenwanger, T., Schmidt, C., Bittner, M., Jacobi, C., Yee, J.-H., Mlynczak, M. G., and Russell III, J. M.: Derivation of gravity wave intrinsic parameters and vertical wavelength using a single scanning OH (3-1) airglow spectrometer. Atmos. Meas. Tech., 11, 2937–2947, doi: 10.5194/amt-11-2937-2018, 2018.
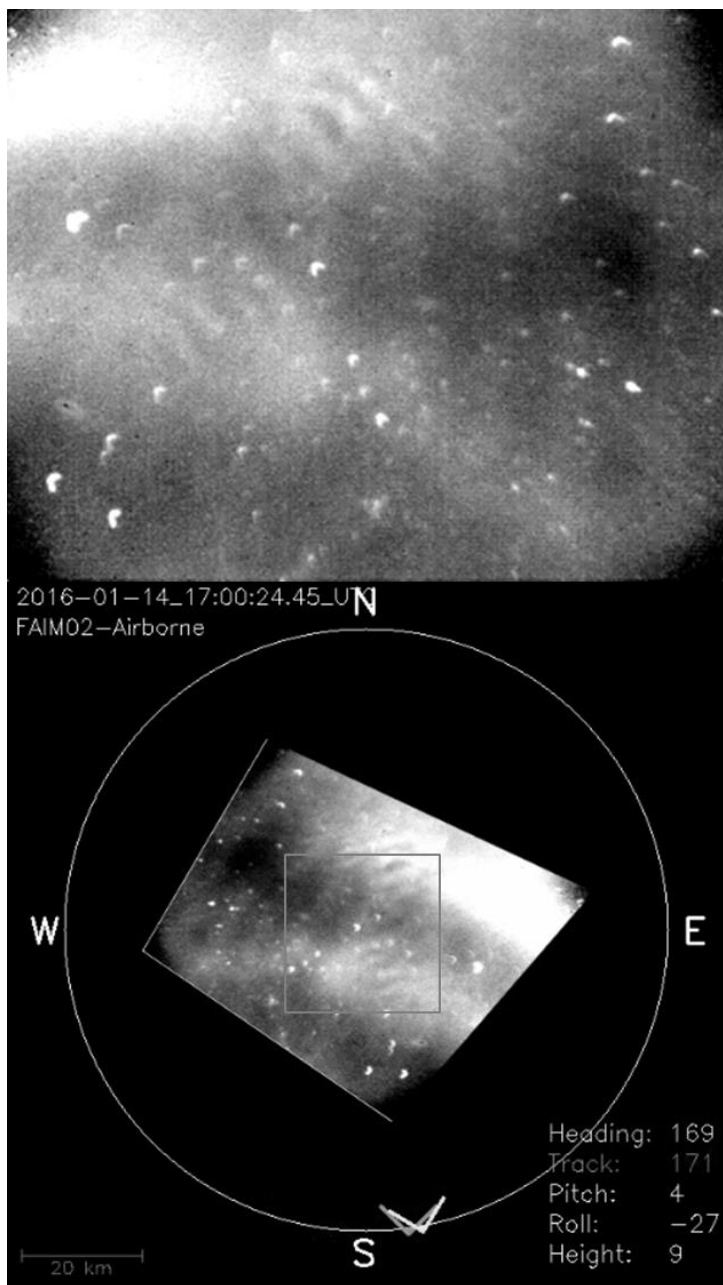
Figure 1: Image from the airborne FAIM 2 imager during the first flight. The top image shows the raw image flat fielded and
contrast adjusted. The bottom image shows the processed image with unwarping due to pitch, roll and yaw angle rotated to a
northward position and mirrored to fit the correct west-east position giving a satellite's view of the airglow layer. The square
marks the region of interest which is used for calculation of the spectral analysis.
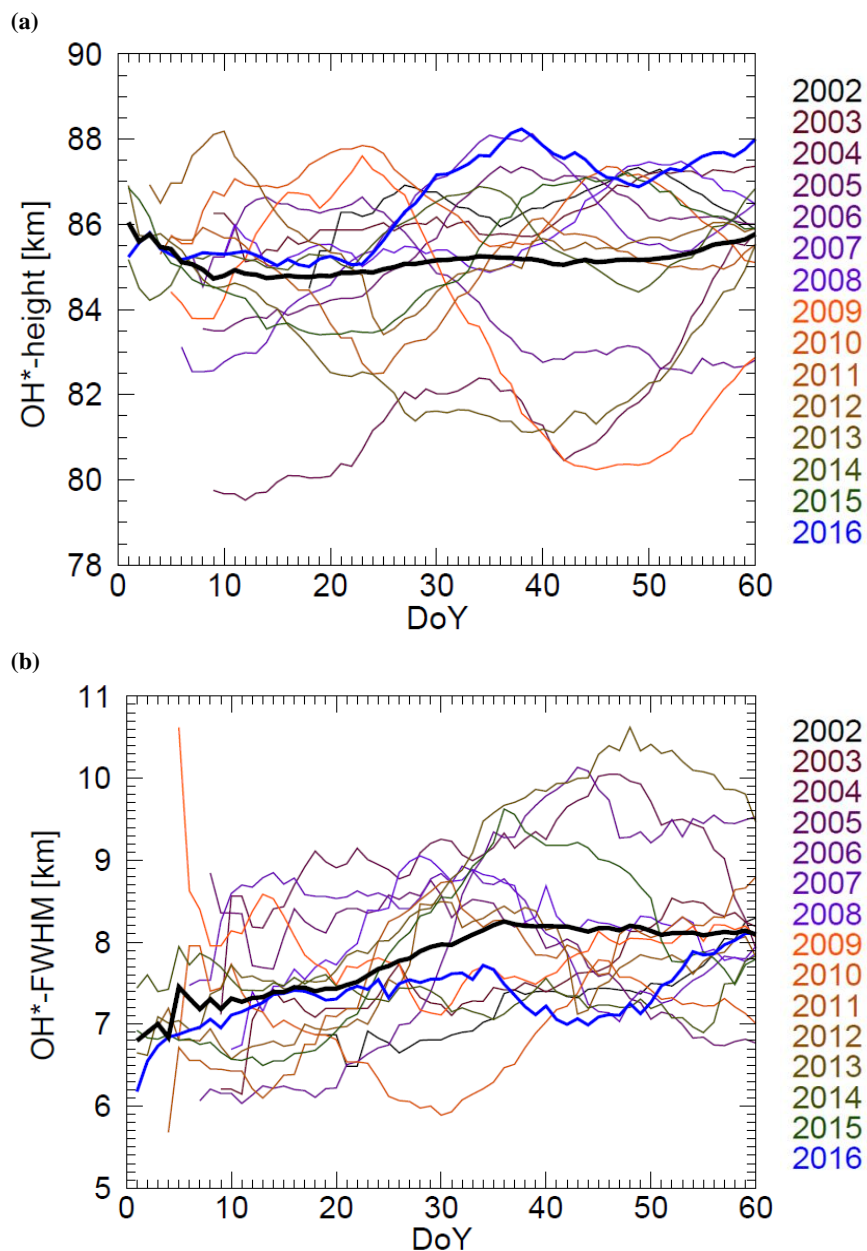
Figure 2: The different curves represent 15-days running means of the OH*-layer height (a) and its FWHM (b) calculated from TIMED-SABER temperature profiles within a rectangle centred at ALOMAR with 300 km edge length. Shown is the time period DoY 1-60 for 2002–2016 (colour-coded, the bold black line is the mean of all years, the bold blue line the year 2016). If more than one value is available per day, a daily mean is calculated before smoothing. However, it can also happen that no SABER measurement is available for a specific day. In this case, the smoothed value of all other valid points within the smoothing window is derived. Due to the yaw cycle of SABER, there is a larger data gap of some 10 days at the end of each year which can also affect the beginning of the subsequent year. This can limit the reliability of the smoothed data at the beginning of the individual years (see e.g. 2009). For 2015, data are available until day 312, in 2016 the time period DoY 5–65 is covered. Therefore, the results are reliable from day 12 until day 58 approximately.

(a)

(b)
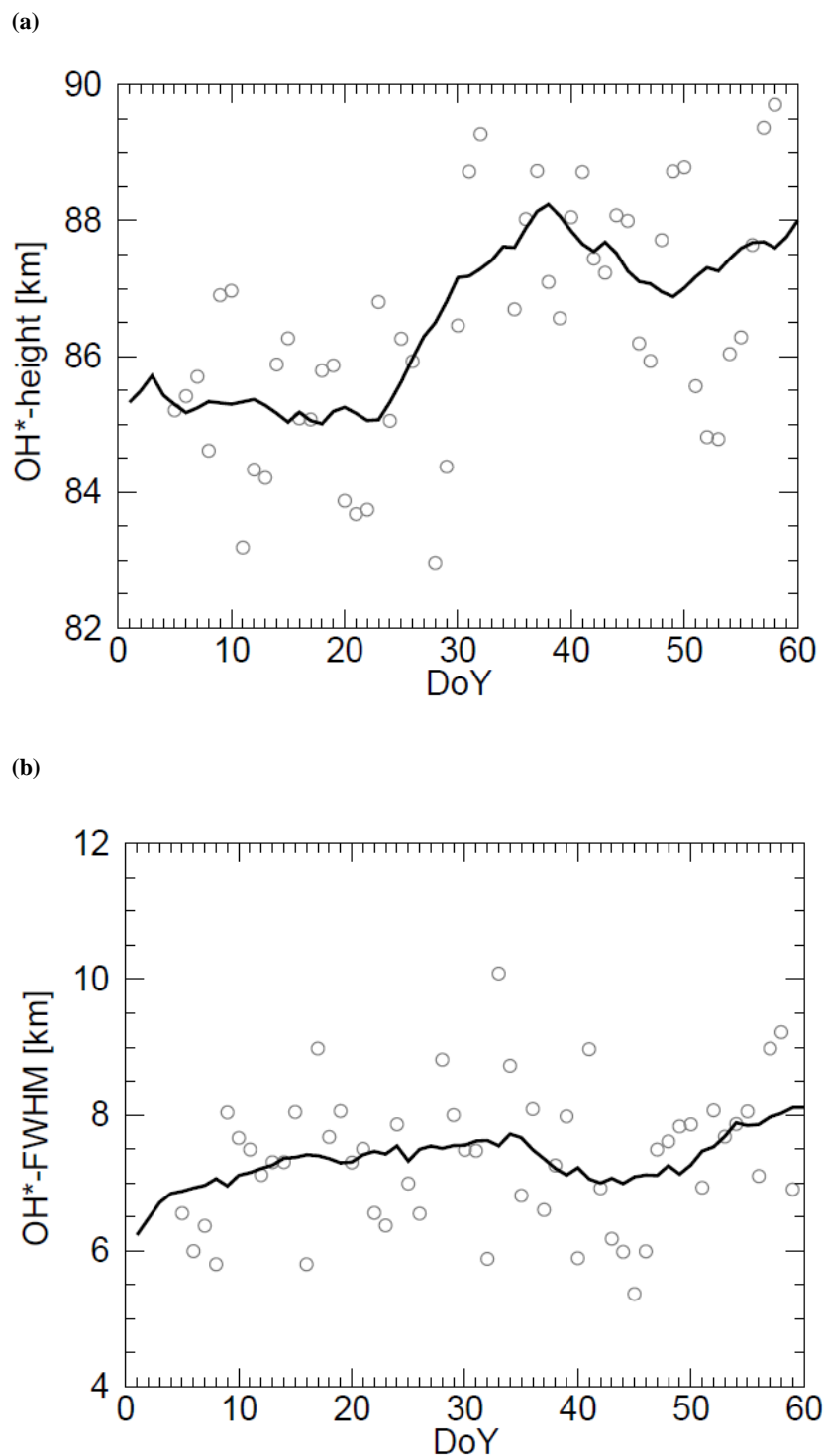
Figure 3: As in Figure 2, the solid lines represent 15-days running means of the OH*-layer height (a) and its FWHM (b). The circles stand for the individual values.
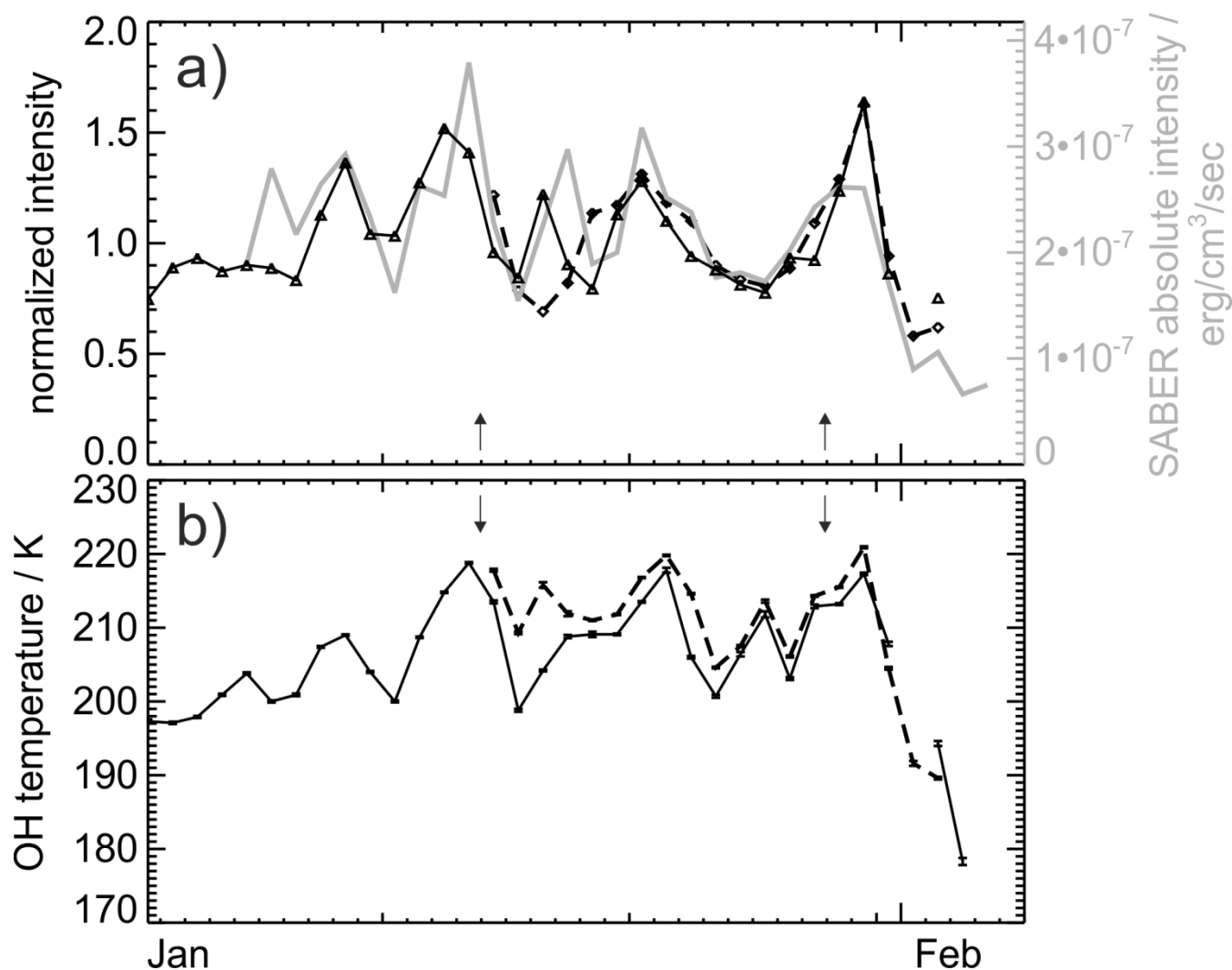
Figure 4: a) Average airglow intensity during the GW-LCYCLE campaign, covered by the three instruments GRIPS 14 at ALOMAR (solid, triangles), GRIPS 9 at Kiruna (dashed, diamonds) and SABER (grey) normalized to the respective mean intensity of the time period. The arrows mark the dates of flight 1 and 5. **b)** Nightly mean OH temperatures at ALOMAR (solid) and Kiruna (dashed). The absolute temperature values agree within 11 K at maximum. This is in the order of magnitude which can be expected for this latitude, distance, and season (see figure 5 from Wendt et al., 2013 for comparison).
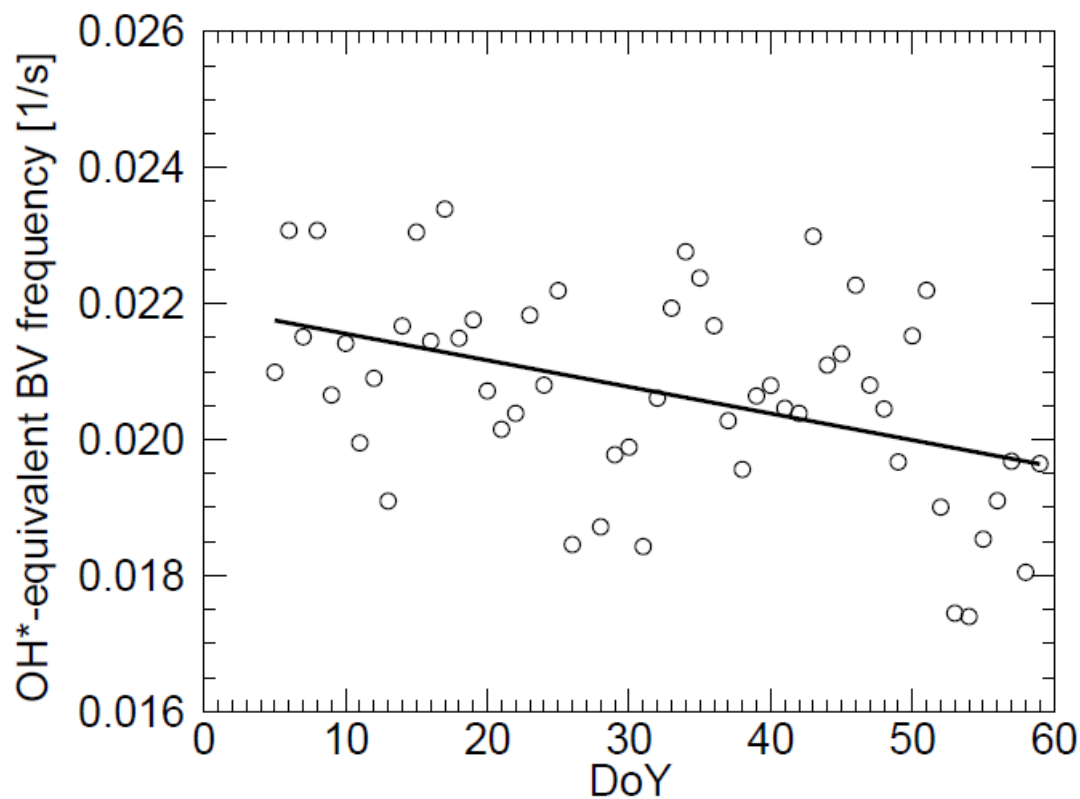
5   **Figure 5: Overall, the OH*-equivalent (angular) Brunt-Väisälä (BV) frequency (circles are individual values) decreases from DoY 1–60 2016 over ALOMAR. The mean difference between the linear fit and the daily OH*-equivalent (angular) Brunt-Väisälä (BV) frequency is ca. 5%.**

(a)

(b)
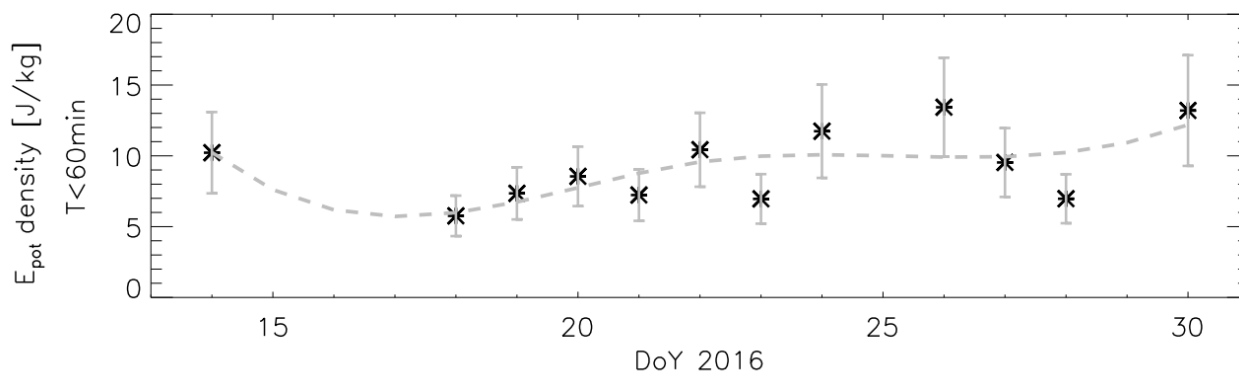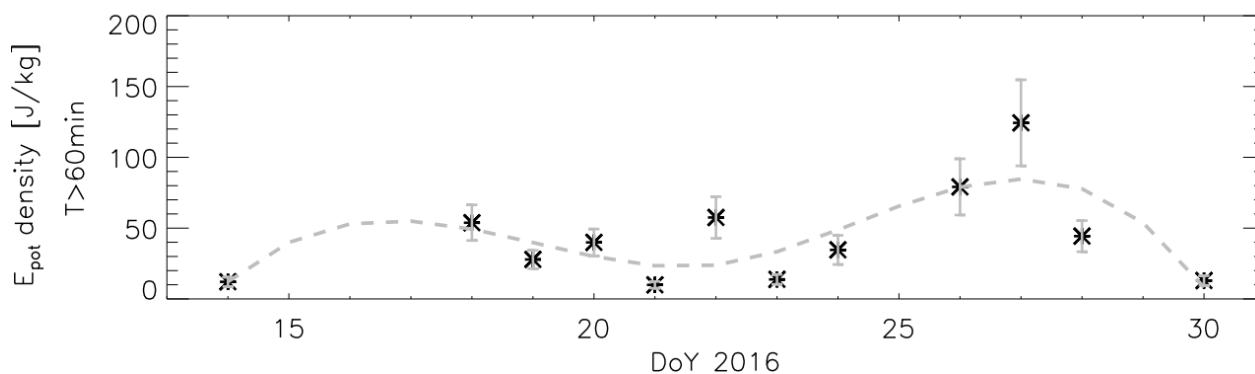
Figure 6 The upper plot shows the nightly mean wave potential energy density for periods shorter than 60 min, while part b refers to periods longer than 60 min. The nightly mean OH*-equivalent (angular) BV frequency was taken from SABER. For the night from January 27th to 28th, coincident SABER profiles were not available, therefore, the mean based on the values of the night before and after was calculated. A cubic spline approximation is superimposed (dashed line).
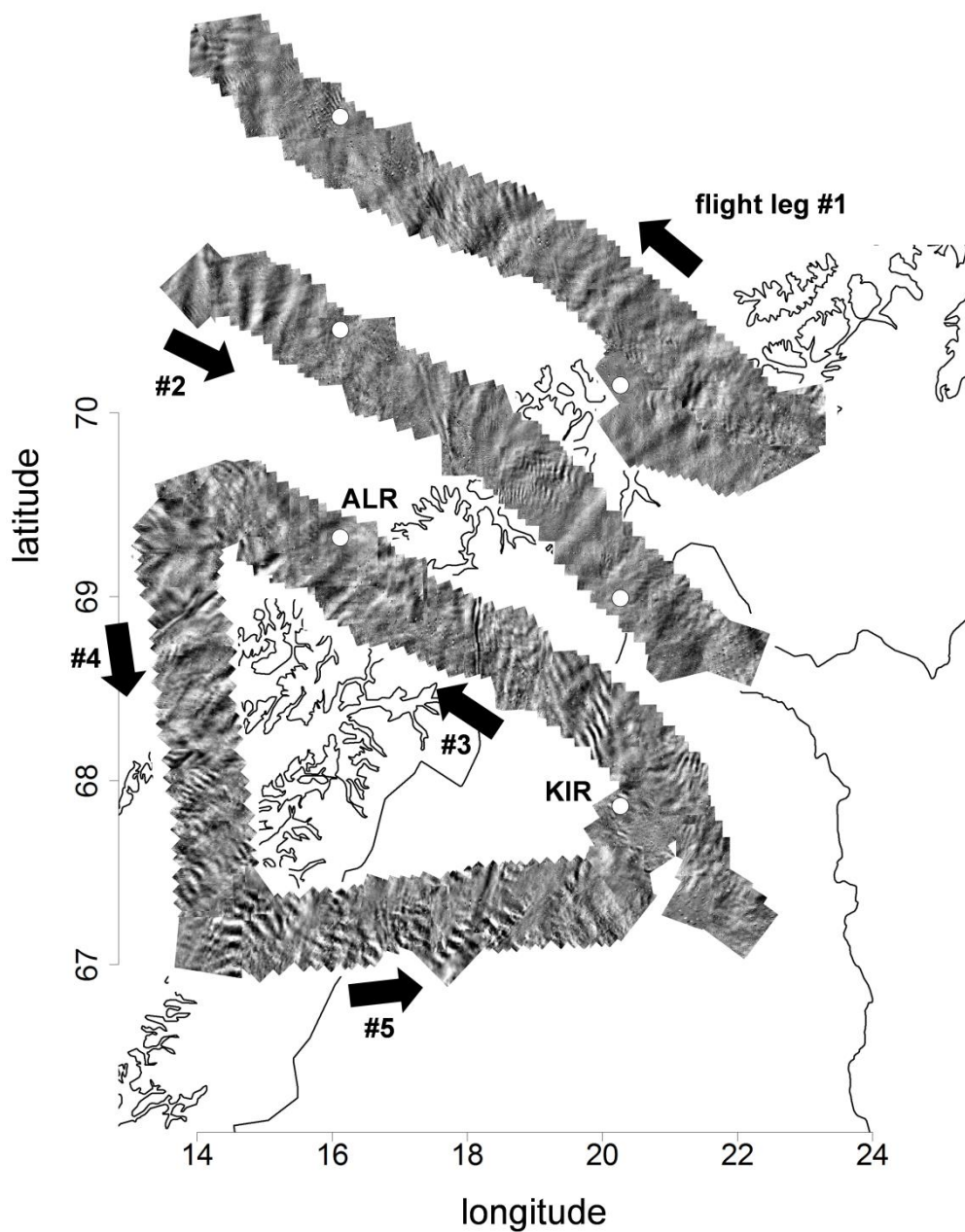
Figure 7: Difference images of the first flight (Jan 14). Please note that the first three legs cover the same area, but legs one and two have been shifted for a better display. Apparently, the small scale structures change rapidly within a few minutes.

(a)

(b)
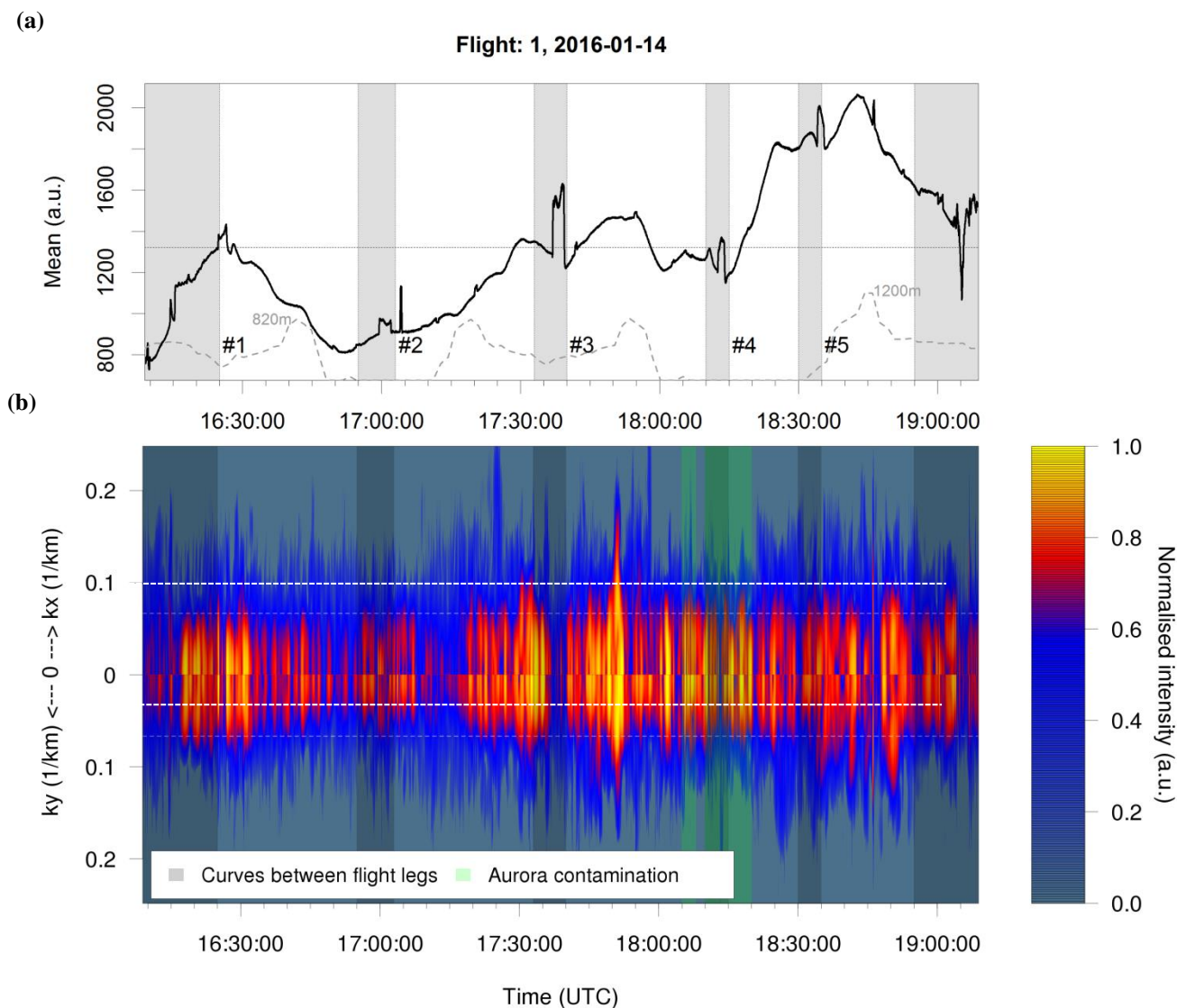
Figure 8 (a) Time series of integrated intensity per FAIM image. The grey areas refer to turning manoeuvres and should be excluded from further analysis. The grey line shows the orography. (b) 2D FFT spectra versus time: in the upper (lower) part the spectral intensity depends on the zonal (meridional) wave number. This plot is created by summing up the significant spectral intensities over the meridional (zonal) wave numbers for each image. The colour bar is normalized in a way that the different spectra are comparable within one flight (logarithm to the basis of 10 is applied to each spectrum, mean and standard deviation over these values of the whole time series are calculated, values higher or lower than the mean plus or minus two times the standard deviation are set to 1 or 0). The horizontal line marks the wavelength of 15 km.

(a)   **(b)**   **(c)**
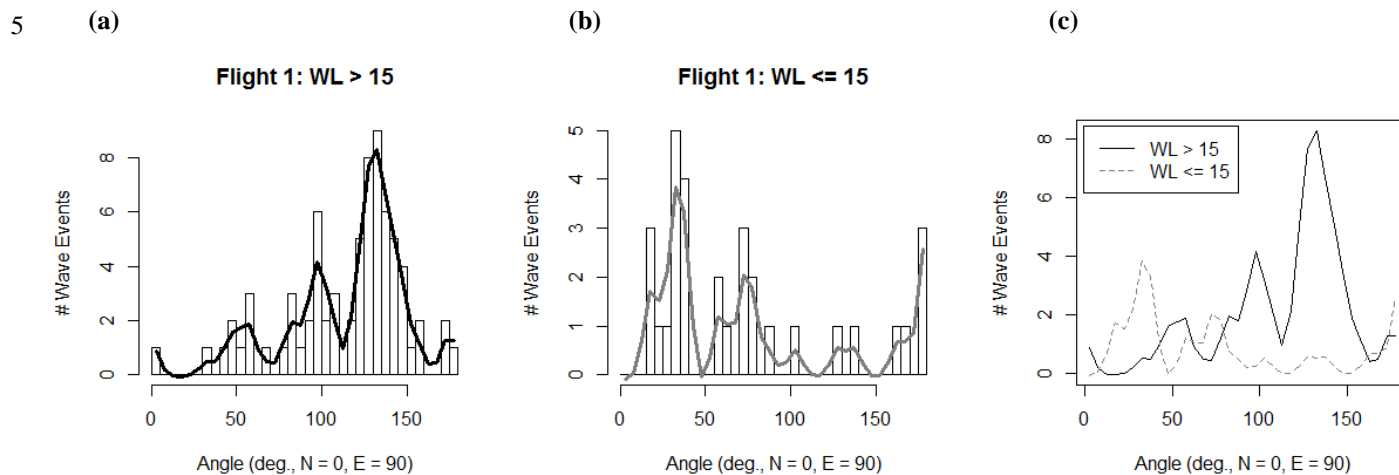
Figure 9 If wavelength and propagation direction are identical for at least six images separated by 30 s at maximum (parameter n), this wavelength is denoted as wave event. Wave events must be present for more than 10 s at least (time difference between first and last occurrence, parameter t). a) and b) depict the histograms of propagation directions (180° ambiguity, 5° bar width) smoothed by a cubic spline for wave events with horizontal wavelengths longer and shorter than 15 km for flight 1. Part c) shows both splines in one plot (black and grey: wavelength longer and shorter than 15 km). Smaller n and t change the absolute values for wavelengths longer than 15 km but not the qualitative results. Wavelengths shorter than 15 km are more sensitive to these parameters (especially to n) but with a stable peak at ca. 40°.
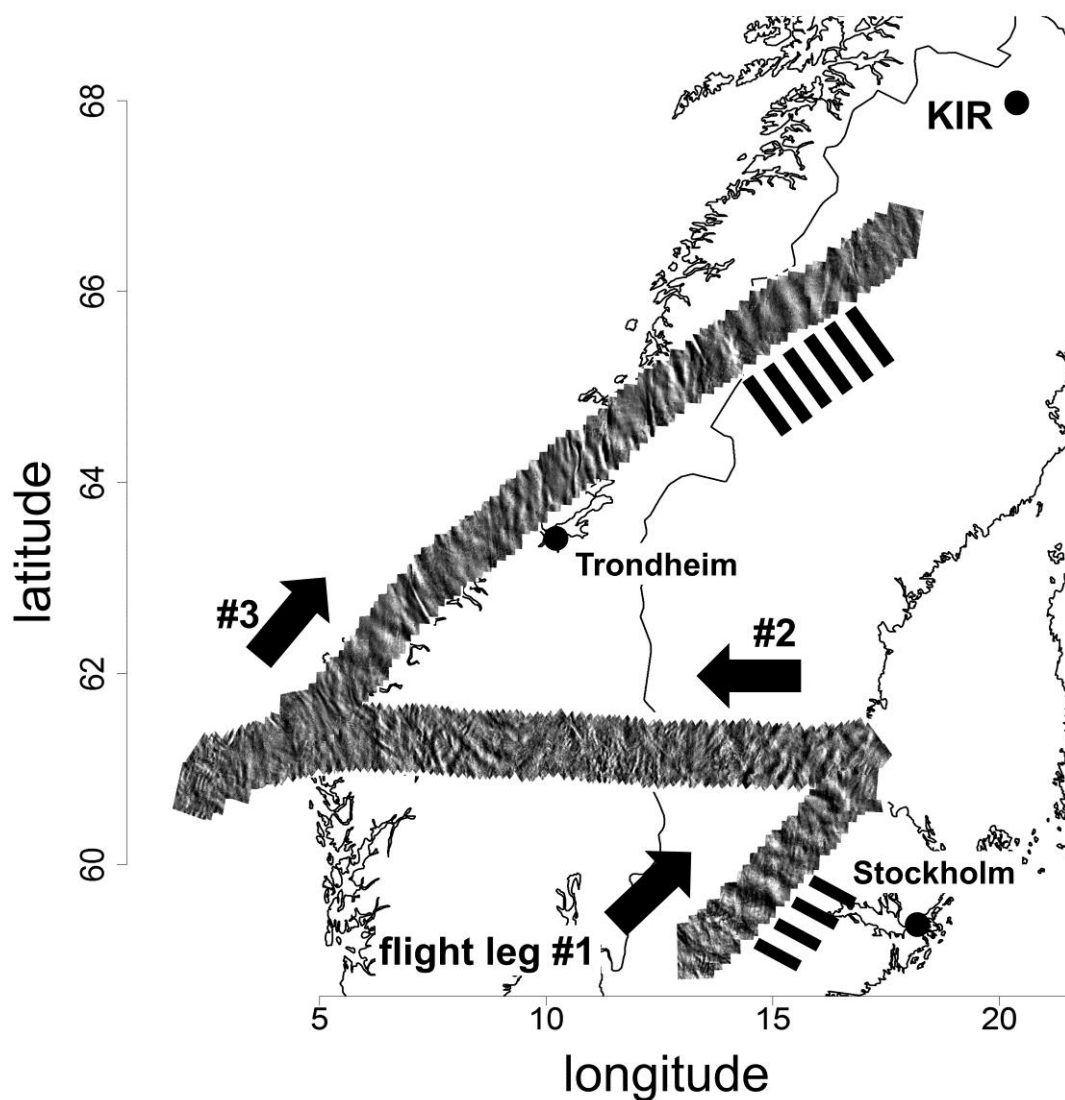
Figure 10: Same as Figure 7 for the second flight of Jan 28, starting in Karlsbad. During the descent to Kiruna, high clouds obstructed the FoV and the respective observations are not shown. The black bars denote the appearance of gravity waves with larger scales than the instantaneous FoV.

(a)

(b)
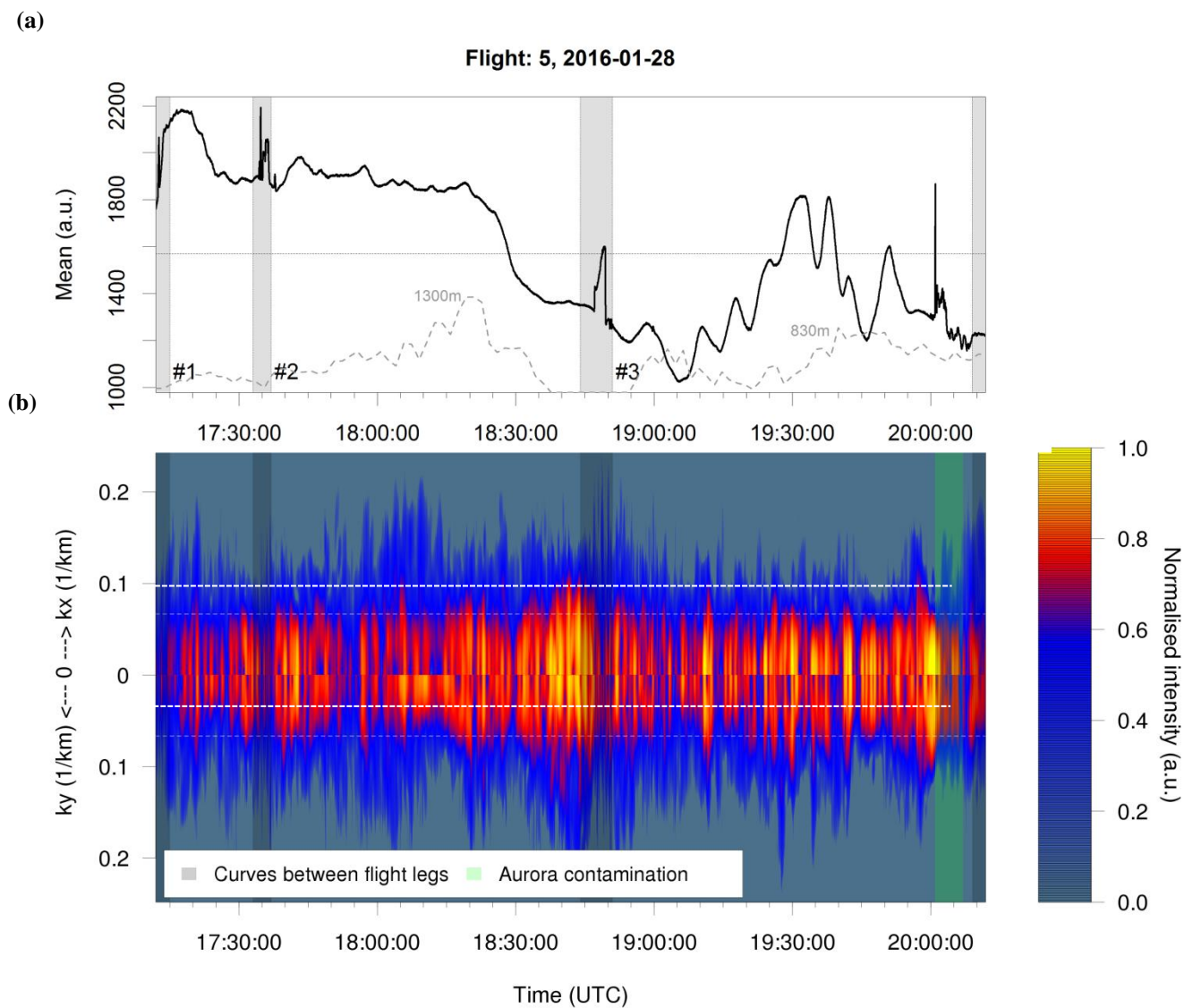
Figure 11 Same as Figure 8 but for flight 5.

(a)   **(b)**   **(c)**
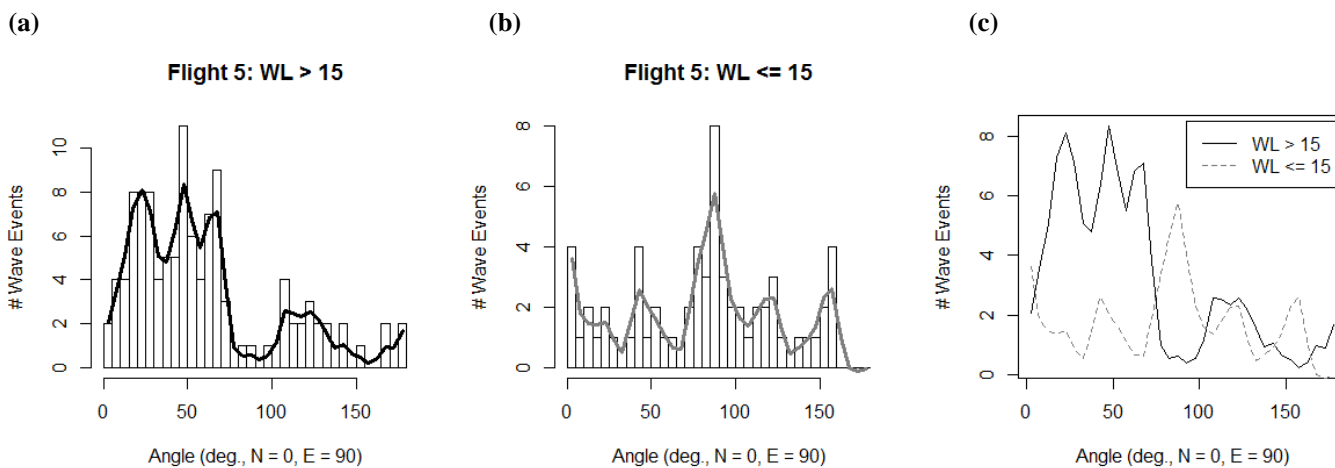
Figure 12 same as Figure 9 but for flight 5. In this case, the results for both wavelength ranges are qualitatively stable for different n and t (the smaller n and t, the higher the absolute values).
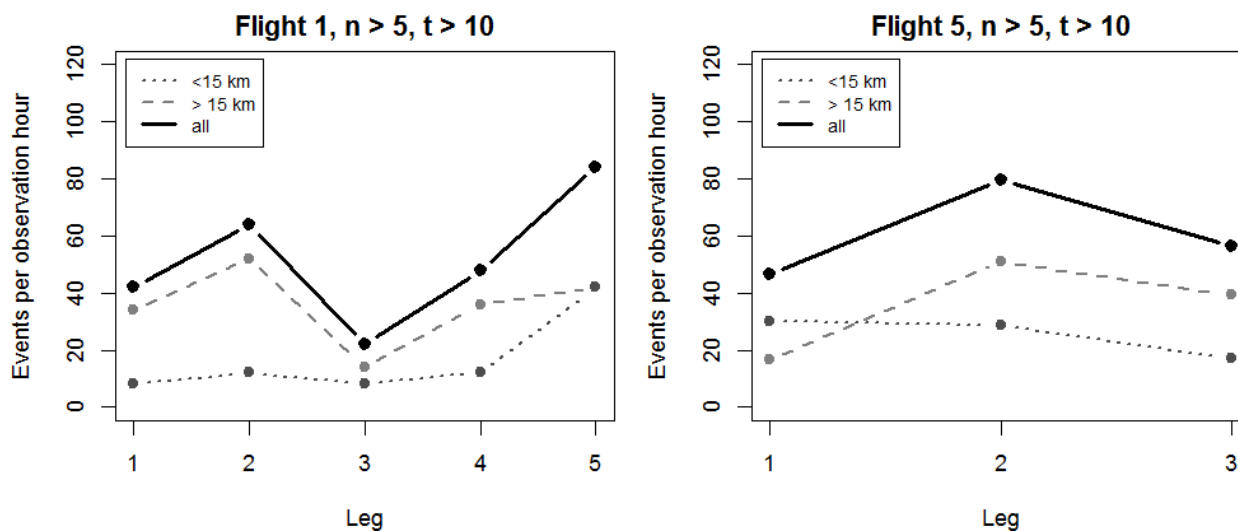
Figure 13 Occurrence rate of significant wave events for each leg of flight 1 and 5 (measurements during turning manoeuvres and aurora events are not included). The results are shown for wavelengths smaller (dotted line) and larger than 15 km (dashed line) as well as for the sum of both (solid line). If wavelength and propagation direction are identical for at least six images (parameter n) separated by 30 s at maximum, this wavelength is denoted as wave event. Wave events must be present for more than 10 s at least (time difference between first and last occurrence, parameter t). The results do not change qualitatively if n and t are smaller.

(a)

(b)
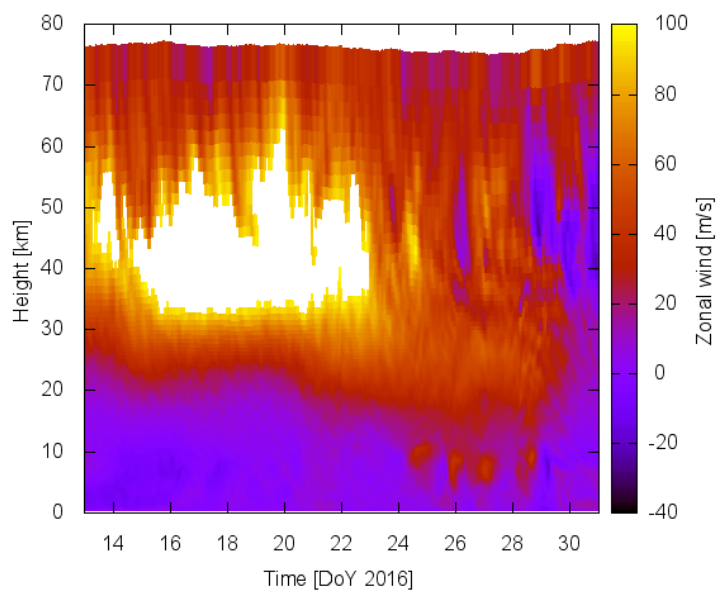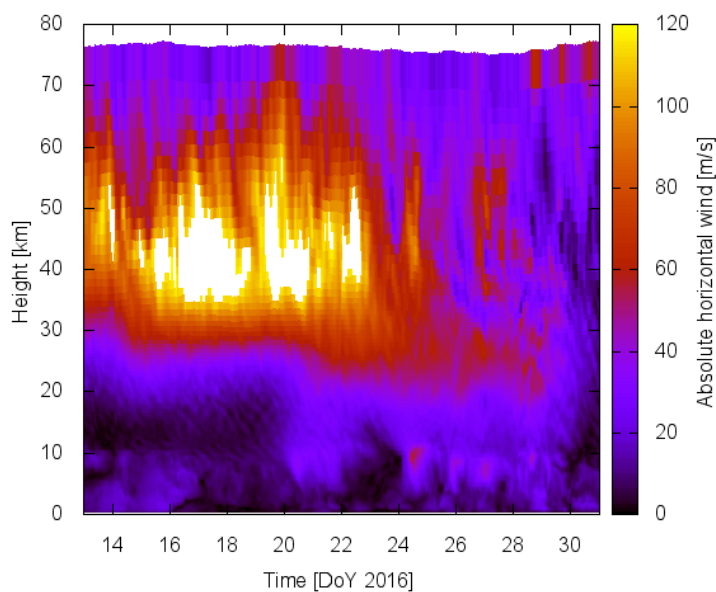
Figure 14 Zonal (a) and absolute horizontal (b) wind at 67.84° N, 20.41° E (Kiruna: 67.86° N, 20.24° E) from ECMWF data (European Centre for Medium-Range Weather Forecast, ECMWF data were provided by Andreas Dörnbrack, DLR).